JOURNAL OF GEOPHYSICAL RESEARCH, VOL. 114, D22205, doi:10.1029/2009JD012353, 2009

Cloud condensation nucleation activity of biomass burning aerosol

Markus D. Petters,[1,2] Christian M. Carrico,[1] Sonia M. Kreidenweis,[1] Anthony J. Prenni,[1] Paul J. DeMott,[1] Jeffrey L. Collett Jr.,[1] and Hans Moosmüller[3]

Received 28 April 2009; revised 13 August 2009; accepted 24 August 2009; published 21 November 2009.

[1] We examine the hygroscopic properties of particles freshly emitted from laboratory biomass burning experiments conducted during the second Fire Lab At Missoula Experiment (FLAME-II). Values of the hygroscopicity parameter, kappa, were derived from both hygroscopic growth measurements and size-resolved (30–300 nm in diameter) cloud condensation nuclei (CCN) measurements for smokes emitted by the open combustion of 24 biomass fuels from the United States and Asia. To analyze the complex cloud condensation nuclei response curves we propose a new inversion scheme that corrects for multiple charge effects without the necessity of prior assumptions about the chemical composition and mixing state of the particles. Kappa varied between 0.02 (weakly hygroscopic) and 0.8 (highly hygroscopic). For individual smokes, kappa was a function of particle size, with 250 nm particles being generally weakly hygroscopic and sub-100 nm particles being more hygroscopic. At any given size the emissions were often externally mixed, showing more and less hygroscopic growth modes and bimodal CCN activation spectra. Comparisons between growth factor-derived and CCN-derived hygroscopicities were consistent when taking this heterogeneity into account. A conceptual model of biomass burning emissions suggests that most particles are CCN active at the point of emission and do not require conversion in the atmosphere to more hygroscopic compositions before they can participate in cloud formation and undergo wet deposition.

Citation: Petters, M. D., C. M. Carrico, S. M. Kreidenweis, A. J. Prenni, P. J. DeMott, J. L. Collett Jr., and H. Moosmüller (2009), Cloud condensation nucleation activity of biomass burning aerosol, *J. Geophys. Res.*, *114*, D22205, doi:10.1029/2009JD012353.

1. Introduction

[2] Biomass burning plays an important role in the global carbon cycle. Deforestation fires alone contribute ~19% to the CO_2 radiative forcing increase since preindustrial times [*Bowman et al.*, 2009]. Aerosols that are emitted simultaneously with greenhouse gases partially offset the resulting warming by scattering sunlight, and can also indirectly affect climate by modifying cloud microphysical properties. For example, clouds in areas with elevated aerosol optical depths stemming predominantly from biomass burning sources have been observed to pass the autoconversion threshold at warmer temperatures [*Lin et al.*, 2006], possibly through the ability of biomass burning aerosol to function as condensation/immersion ice nuclei [*Petters et al.*, 2009a] or as deposition ice nuclei [*Sassen and Khvorostyanov*, 2008]. Studies of fire-dominated air masses in the Amazon basin and Texas suggest that fires also modify the droplet number concentration in cumulus clouds by emitting cloud condensation nuclei [*Andreae et al.*, 2004; *Kaufmann et al.*, 1998; *Lee et al.*, 2006; *Rissler et al.*, 2006; *Ross et al.*, 2003; *Vestin et al.*, 2007].

[3] To date few studies have investigated cloud condensation nuclei activity of biomass burning aerosol under controlled laboratory conditions. Many studies have focused on investigating single component organic compounds that have been identified on filter samples. Among the studied compounds thus far are dicarboxylic acids [*Prenni et al.*, 2001], saccharides [*Rosenørn et al.*, 2006; *Svenningsson et al.*, 2006], and benzoic acids [*Huff Hartz et al.*, 2006; *Mochida and Kawamura*, 2004]. To our knowledge only two studies generated actual smoke particles from biomass fuels in the laboratory [*Dusek et al.*, 2005; *Novakov and Corrigan*, 1996]. Here we build on these studies and report on hygroscopic growth factors and cloud condensation nuclei activity of biomass burning aerosols generated from 24 individual biomass fuels originating from various regions of the United States and Asia. Because smoke aerosols are often externally mixed and their size resolved mixing state is not known a priori, the interpretation of the measured CCN activation spectra is not as straightforward as for other aerosols that are generated via homogeneous nucleation or atomization. To address this issue we propose an inversion technique that builds on the method described by *Petters et al.* [2007]. Using this inversion we infer hygroscopicity parameters [*Petters and Kreidenweis*,

[1]Department of Atmospheric Science, Colorado State University, Fort Collins, Colorado, USA.
[2]Now at Department of Marine Earth and Atmospheric Sciences, North Carolina State University, Raleigh, North Carolina, USA.
[3]Desert Research Institute, Nevada System of Higher Education, Reno, Nevada, USA.

0148-0227/09/2009JD012353$09.00

2007] for each of the smokes and characterize the heterogeneity of the hygroscopic response for these fuels. These data are used to deduce the overall CCN activity of fresh biomass burning emissions.

2. Experimental Methods

2.1. Hygroscopicity

[4] The Köhler equation relates the saturation ratio, $S = RH/100$, to water activity and the Kelvin term

$$S = a_w \exp\left(\frac{4\sigma_{s/a}M_w}{RT\rho_w D}\right) \quad (1)$$

where a_w is the activity of water in solution, ρ_w is the density of water, M_w is the molecular weight of water, $\sigma_{s/a}$ is the surface tension of the solution/air interface, R is the universal gas constant, T is the temperature, and D is the diameter of the droplet. To parameterize the solution water activity, we use the single parameter representation of *Petters and Kreidenweis* [2007] who defined the hygroscopicity parameter κ as

$$a_w^{-1} = 1 + \kappa\frac{V_s}{V_w}, \quad (2)$$

where V_s is the volume of the dry particulate matter and V_w is the volume of the water. Using equation (2), *Petters and Kreidenweis* [2007] showed that the Köhler curve is given by

$$S(D) = \frac{D^3 - D_d^3}{D^3 - D_d^3(1-\kappa)} \exp\left(\frac{\Psi}{D}\right) \quad (3)$$

where $\psi = 2.1 \times 10^{-9}$ m is a constant that is evaluated at $T = 298.15$ K and the solution surface tension of water, $\sigma_{s/a} = 0.072$ J m^{-2}. The critical supersaturation (s_c, where $s_c = S_c - 1$ and is usually expressed as a percentage) for a selected dry diameter of a particle having hygroscopicity κ is computed from the maximum of equation (3). Alternatively, to find κ for an observed pair of s_c–D_d we hold D_d constant and iteratively vary κ until the maximum in equation (3) is equal to s_c. Kappa also can be obtained from hygroscopic size growth factors, $gf = D/D_d$, measured with a humidified tandem differential mobility analyzer (HTDMA). Hygroscopicity and growth factors are related via

$$\kappa = \left(gf^3 - 1\right)\left(a_w^{-1} - 1\right), \quad (4)$$

where a_w is obtained from equation (1).

2.2. Smoke Generation

[5] The FLAME II study was carried out in May/June 2007 at the United States Department of Agriculture U.S. Forest Service Fire Science Lab in Missoula, MT. Details about the combustion facility, fuels used, combustion, sampling, and analytical procedures are described elsewhere [*McMeeking*, 2008; *Petters et al.*, 2009a]. The FLAME study was targeted to close gaps in aerosol and gas-phase emissions inventories for open biomass burning [*McMeeking et al.*, 2009]. The fuels selected for this study were representative of those burned in wild and prescribed fires throughout the western and southeastern United States and were chosen on modeled frequency of fuels burned in fire-impacted regions, prioritizing on species with little or no peer-reviewed emission data available [*McMeeking et al.*, 2009]. The names of fuels, their location of collection, and the part of the plant that was burned are summarized in Table 1. Unless noted otherwise the entire plant was burned, i.e., a composite of leaves and woody material. If specific parts of the plant were burned we include this part after giving the name of the fuel, e.g., gallberry (leaves + stems). For some burns mixtures of fuels were selected. Burns were performed on a combustion platform, illustrated in Figure 1, which consisted of a ceramic tile lined with resistive heating wire and sheathed in a Thermeez 395 woven ceramic sleeving that was soaked in 15 g of ethanol. The ceramic tile was placed on a Mettler PM34 microbalance and loaded with 30–500 g of fuel. A voltage was applied to the heating wire, resulting in a uniform ignition of the fuel bed followed by 5–10 min flaming and smoldering fire phases.

[6] Two smoke sampling strategies were implemented during the study, termed "chamber burns" and "stack burns." During the chamber burns the entire burn chamber, a large room with dimensions 12.4 m × 12.4 m × 19.6 m, was allowed to fill with smoke. Before the burns the room was vented with ambient air, and then closed for the duration of the experiment, including the burn itself and the sampling period. An inlet consisting of a 1″ (25 mm) inner diameter stainless steel tube was used to pull sample into an adjacent laboratory and into our instruments. Smokes were continuously sampled from the burn chamber over ~2–3 h after the combustion was completed. In the stack burns the combustion emissions were vented through an exhaust stack that was directly located above the fuel bed. A 1.5" (32 mm) inner diameter stainless steel tube was inserted into the center of the exhaust stack at a height of approximately 16 m above the fuel bed and connected to a 200 L stainless steel sampling drum placed ~20 m downstream of the inlet. The smoke temperature at the top of the stack varies from fire to fire but the maximum typically does not exceed 90°C [*Christian et al.*, 2003]. The drum was filled with smoke from the exhaust stack using a high volume air pump (Gast Mfg. Model R1102, 300 Lpm). After collection, the inlet to the drum was sealed and the outlet was connected to a preconditioning system that drew 3 Lpm sample from the drum. During measurements, the drum was open to the room through a HEPA filter to prevent depressurization.

[7] The purpose of the chamber burns was to sample more dilute smokes over longer periods of time. This strategy was particularly important for the sampling of the optical properties of the aerosol, data that we do not report here. Conversely, the motivation for the stack burns was to sample as many burns as possible within a short period of time, at high aerosol mass concentrations [*McMeeking et al.*, 2009].

2.3. Particle Preconditioning

[8] Prior to the measurement the sample flow was humidified to >95% RH and then dried to $RH < 5\%$. This was done to collapse particles with large fractal dimensions

Table 1. Alphabetical List of Fuels Used in This Study[a]

Common Name	Genus or Species	Country or State	Part of Plant Burned
Black spruce	Picea mariana	Alaska N64° 37′ W148° 43′	needles
Ceanothus	Ceanothus crassifolius	California N33° 50′ W116° 52′	plant
Chamise	Adenostoma fasciculatum	California N33° 50′ W116° 52′	plant
Common reed	Phragmites australis	Louisiana N29° 58′ W93° 5′	plant
Douglas fir	Pseudotsuga menziesii	Montana N46° W114°	needles, branches, needles + branches, dry needles, dry branches
Duff	Pleurozium schreberi	Alaska	uppermost layer of soil with live and dead feathermoss
Gallberry	Ilex coriacea Ilex glabra	Florida N30° 6′ W84° 16′ Mississippi N30° 13′ W82° 24′	leaves + stems
Hickory	*Carya nutt*	North Carolina N36° 6′ W79° 6′	leaves
Kudzu	Pueraria Montana	Georgia N33° 55′ W83° 23′	plant
Longleaf pine	Pinus palustris	Florida N30° 3′ W84° 24′	needles + sticks
Manzanita	Arctostaphylos glandulosa	California N33° 52′ W116° 52′	branches
Needlegrass rush	Juncus roemerianus	North Carolina	plant
Oak	Quercus laevis	North Carolina N36° 6′ W79° 6′	leaves
Palmetto	Serenoa repens	Florida N30° 3′ W84° 24′ Mississippi N30° 27′ W88° 39′	leaves
Ponderosa pine	Pinus ponderosa	Montana	needles + sticks
Rhododendron	Rhododendron minus	Montana	plant
Rice straw	Oryza sativa	Taiwan	plant
Sagebrush	Artemisia tridentate	Utah N41° W112° Montana	plant
Sugarcane	Saccharum officenarum	Taiwan	plant
Swamp sawgrass	Cladium mariscus	N30° 17′ W89° 55′	plant
Titi	Cyrilla racemiflora	Florida N30° 9′ W84° 13′	plant
Wax myrtle	Myrica cerifera	Mississipi	plant
White spruce	Picea glauca	Alaska N64° 51′ W147° 28′	plant
Wiregrass	Aristida beyrichiana	Florida N30° 6′ W84° 16′	plant

[a]Fuel names are given as common name, and as scientific name where the genus is in italic and the species is in nonitalic font. Numbers below the state or country give latitude and longitude in degrees and minutes where available. The term "plant" denotes that a part of the plant, representative of its aboveground biomass, was burned.

[*Chakrabarty et al.*, 2006; *Lewis et al.*, 2009] and the system is described further by *Petters et al.* [2009a]. The resulting polydisperse size distribution was diluted with dry, filtered air in an 11 L stainless steel mixing chamber and the sample flow was charge neutralized using eight newly manufactured 500 μCi ^{210}Po charge strips. The charge neutralized sample flow was diluted in a mixing chamber and split to a cloud condensation nuclei counter to measure size-resolved CCN concentrations (Droplet Measurement Technologies, DMT [*Lance et al.*, 2006; *Roberts and Nenes*, 2005; *Rose et al.*, 2008a]), and an HTDMA to measure size growth factors. These measurements are dscribed further below.

2.4. Hygroscopic Growth Measurements

[9] The HTDMA used in these studies is described by *Carrico et al.* [2008] and consists of two differential mobility analyzers (DMA, TSI 3080), two condensation particle counters (CPC, TSI 3010), and a humidification system. The first DMA (sheath-to-sample flow ratio of 5:1) selects a quasi-monodisperse distribution of smoke particles according to their dry electrical mobility diameters (D_d). Following size selection the particle flow is humidified and a second DMA discretely steps through voltages to measure the humidified particle size distribution. The wet size distribution after humidification was inverted using the algorithm of *Zhou et al.* [2002] to find the peak wet diameter D, from which the growth factor and κ were calculated. This inversion algorithm is a multimodal implementation of the TDMAfit method developed by *Stolzenburg and McMurry* [1988].

2.5. CCN Measurements

[10] Our CCN setup involves scanning through dry particle diameter while keeping the supersaturation in the CCN instrument fixed; the method is described in detail by *Petters et al.* [2007]. Briefly, charge-equilibrated particles were mobility-selected using a DMA (TSI 3071) and processed in a DMT CCN counter, while simultaneously the total particle concentration transmitted to the CCN instrument was measured using a condensation particle counter (TSI 3010). No impactor was used upstream of the DMA; this introduces some uncertainty in the inversion discussed below. The CCN instrument was operated at 0.5 Lpm total flow rate and 10:1 sheath-to-sample flow rate ratio. The streamwise temperature differences were set by the instrument software to be 5.41 K and 8.49 K. The supersaturations were calibrated daily using CCNc response curves for atomized, dried, charge-neutralized, and size-selected ammonium sulfate particles. To find the supersaturation for a given temperature gradient in the CCN instrument the measured activation diameter for ammonium sulfate particles was converted to a critical supersaturation using $\kappa = 0.6$ [*Petters and Kreidenweis*, 2007], which is inferred from the critical supersaturation/dry diameter relationship calculated from classical Köhler theory using the water activity data from the Aerosol Inorganic Model (AIM) [*Clegg et al.*, 1998; *Kreidenweis et al.*, 2005, Table 2]. For the temperature differences used here, measured ammonium sulfate activation diameters varied between 48 nm and 67 nm. The corresponding critical supersaturations derived from AIM are 0.27% and 0.46% and the equivalent κ values are 0.59 and 0.61, respectively. Over the course of the project

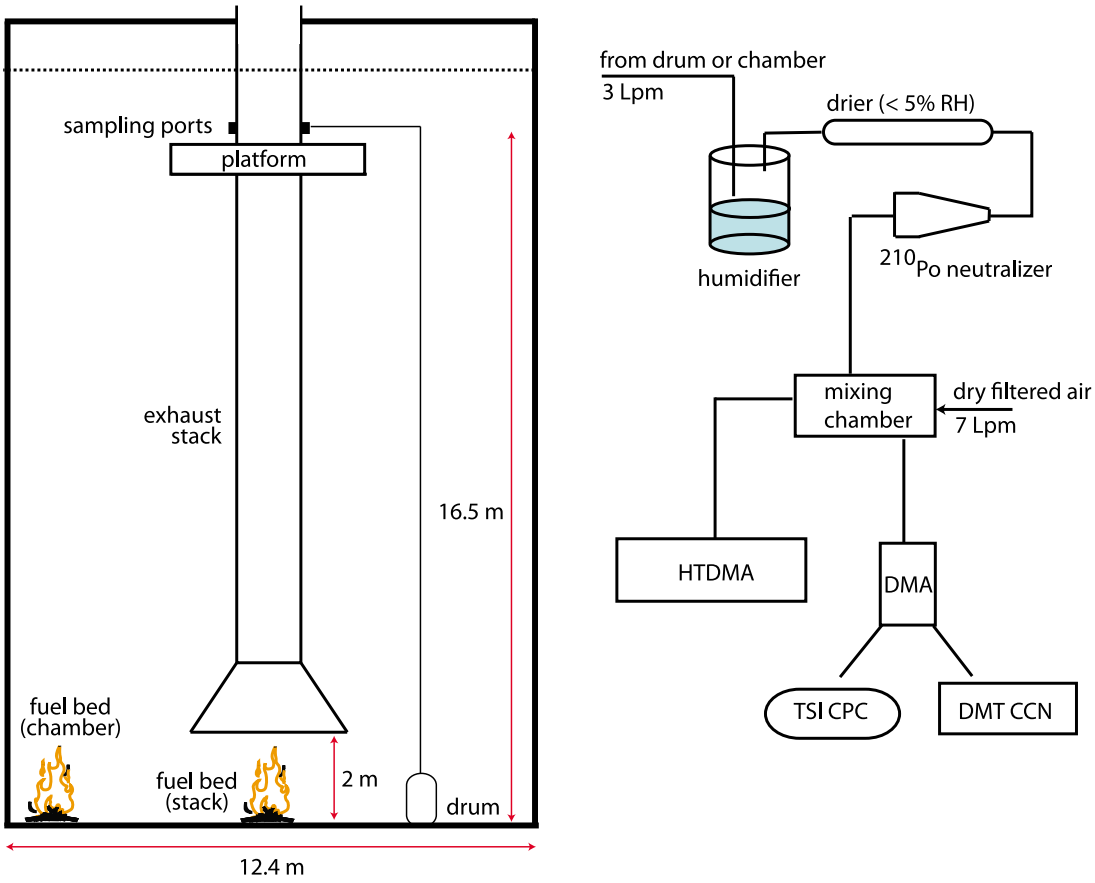

Figure 1. Schematic of the experimental setup. (left) Schematic of the Missoula Fire Science laboratory. (right) Aerosol sampling strategy. Several other instruments also sampled from the mixing chamber but are not included in the schematic.

20 ammonium sulfate response curves were collected, ranging from 0 to 2 per day. Data for each day's experiments were processed using the calibration closest in time. Multiple calibration curves were used to evaluate the uncertainty of the measurement in κ space, resulting in $0.54 < \kappa < 0.64$ due to fluctuations of the instrument supersaturation. This range is somewhat larger than what is obtained for typical laboratory studies, likely due to larger than usual fluctuations of temperature in the Fire Science Laboratory (the supersaturation depends on the inlet temperature [*Roberts and Nenes*, 2005] but this dependence is not accounted for in the data processing). The electrostatic classifier (TSI 3071) was operated at a 10:1.5 sheath-to-monodisperse flow ratio and was used to size select particles prior to the CCN measurement. We scanned through 30 geometrically stepped dry diameters ranging from 30 to 300 nm. For each size, the voltage was held constant for 40s. During data processing, we selected a 30 s subset of each interval to calculate the average CN and CCN response for each voltage.

2.6. CCNc Inversion

[11] The measured response vectors, i.e., instrument reported CN or CCN concentrations as functions of size, must be inverted to find the true aerosol and CCN size distribution. Many DMA inversion algorithms have been proposed in the literature, each valid for a certain experimental setup [e.g., *Alofs and Balakumar*, 1982; *Collins et al.*, 2002; *Gysel et al.*, 2009; *Stratmann et al.*, 1997]. Here we follow the generalized inversion approach described by *Kandlikar and Ramachandran* [1999]. The instrument response in the ith channel is given by the Fredholm integral equation of the first kind

$$R_i = \int_{D_a}^{D_b} \sum_{k=1}^{m} K_i(D_k) P_k(D) g(D) \frac{dN}{dD} dD + \varepsilon_i, \qquad i = 1, 2, \ldots n \tag{5}$$

where R_i denotes the response in the ith instrument channel (number concentration per unit volume), D_k is the physical diameter (unit length) corresponding to a spherical particle, k denotes the number of charges, D_a and D_b are the diameter limits within which the size distribution lies, K_i is the kernel function of the ith instrument channel (dimensionless), $P_k(D)$ is the probability of D carrying k charges (dimensionless), $g(D)$ is the detection efficiency for a particle of size D (dimensionless), dN/dD is the particle size distribution (number concentration per unit volume and unit length), and ε_i is the instrument error in that channel (number concentration per unit volume). Neglecting the error in the measurement (i.e., $\varepsilon_i = 0$) equation (5) can be approximated by expressing the integral as a discrete sum by substituting dD with ΔD_j. The number of particles in the jth

mobility bin is $N_j = \frac{dN}{dD}\Delta D_j$ and equation (5) is approximated by $R_i \approx \sum_{j=1}^{n}\left[\sum_{k=1}^{m} K_i(D_{j,k})P_k(D_j)g(D_j)N_j\right]$ where $D_{j,k}$ denotes the diameter appearing in the ith channel carrying k charges. The indices can be understood as follows: 1) $i = 1\ldots$n indexes the observed instrument channel, here specifically the raw voltage bins and instrument responses R_i; 2) $j = 1\ldots$n indexes the physical size bins; and 3) $k = 1\ldots$m indexes the number of charges carried by the particle. The kernel functions $K_i(D_{j,k})$ and the charging probabilities $P_k(D_j)$ are calculated using standard DMA theory [*Knutson and Whitby*, 1975] and empirical charge equilibrium curves [*Wiedensohler*, 1988] with the correct coefficients obtained from the most recent TSI 3081 DMA manual. Functional forms for K_i $(D_{j,k})$ and $P_k(D_j)$ are given in Appendix A. For readability we define $A_i(D_j) = \sum_{k=1}^{m} K_i(D_{j,k})P_k(D_j)$. Dividing the interval $[D_a, D_b]$ into n intervals leads to a linear set of n equations with n unknowns

$$\begin{aligned} R_1 &\approx \sum_{j=1}^{n} A_1(D_j)g(D_j)N_j \\ R_2 &\approx \sum_{j=1}^{n} A_2(D_j)g(D_j)N_j \\ &\vdots \\ R_n &\approx \sum_{j=1}^{n} A_n(D_j)g(D_j)N_j \end{aligned}. \tag{6}$$

In matrix form equation (6) can be written as

$$\mathbf{R} = \mathbf{A}(\mathbf{g} \circ \mathbf{N}) \tag{7}$$

where $\mathbf{R}$ is a vector of n response measurements, $\mathbf{g}$ is a vector of detector efficiencies, $\mathbf{N}$ is a vector of number concentrations, $\mathbf{A}$ is the $n \times n$ inversion matrix defined in Appendix A, and $\circ$ means the Hadamard product. The Hadamard product is the elementwise multiplication of two matrices/vectors and when applied to two vectors of identical dimension the result is a vector of the same dimension as the original vectors. We note that $\mathbf{g}$ is usually part of the inversion matrix and we intentionally excluded it from the matrix here for reasons that will be explained below. For a measured response vector $\mathbf{R}$ the vector resulting from the elementwise product $\mathbf{g} \circ \mathbf{N}$ can be obtained from a simple matrix inversion

$$\mathbf{g} \circ \mathbf{N} = \mathbf{A}^{-1}\mathbf{R} \tag{8}$$

There is no conceptual difference between using a CN or a CCN instrument to measure a response function, $\mathbf{R}_{CN}$ or $\mathbf{R}_{CCN}$, respectively. Here we use particle diameters $D >$ 30 nm and for those the condensation particle counter detection efficiency is unity, and thus, $\mathbf{g}_{CN} = 1$. In that case

$$\mathbf{N}_{CN} = \mathbf{A}^{-1}\mathbf{R}_{CN}. \tag{9}$$

The detector efficiency $\mathbf{g}_{CCN}$ is not known a priori and the form of $\mathbf{g}_{CCN}$ depends on the ability of the particles to activate as cloud droplets, which encompasses particle size, shape, and composition, and the transfer function of the CCN instrument. For an idealized CCN instrument all particles larger than the activation diameter, D_c, will activate into cloud droplets and particles smaller than D_c will not. Thus $\mathbf{g}_{CCN}$ $(D \geq D_c) = 1$ and $\mathbf{g}_{CCN}(D < D_c) = 0$. The advantage of the matrix inversion approach over the forward calculation used by *Petters et al.* [2007] is that $\mathbf{g}_{CCN}$ can be calculated if $\mathbf{N}_{CN}$ is known

$$\mathbf{g}_{CCN} = \left(\mathbf{A}^{-1}\mathbf{R}_{CCN}\right) \div \mathbf{N}_{CN} = \left(\mathbf{A}^{-1}\mathbf{R}_{CCN}\right) \div \left(\mathbf{A}^{-1}\mathbf{R}_{CN}\right) \tag{10}$$

Here $\mathbf{g}_{CCN}$ defines the CCNc response curve and $\div$ means Hadamard division (elementwise division). We point out that the matrix can be used to perform the forward fitting procedure discussed by *Petters et al.* [2007]. In that method, the size distribution must be known and $\mathbf{g}_{CCN}(D \geq D_c) = 1$ and $\mathbf{g}_{CCN}(D < D_c) = 0$ is applied to the size distribution to calculate the CCN distribution. The expected uncorrected CCN activation spectrum can then be calculated from $(\mathbf{AN}_{CCN}) \div (\mathbf{AN}_{CN})$ and the activation diameter is found by varying D_c until the χ^2 statistic of the observed and predicted uncorrected activation spectra is minimized. The magnitude of the correction from the inversion depends on the aerosol size distribution and the activation diameter and we refer to *Petters et al.* [2007] for those details. The vector $\mathbf{g}_{CCN}$ contains contributions from the nonidealities not captured by the DMA inversion matrix, e.g., nontriangular transfer functions, nonequilibrium charging, contributions from the transfer function of the CCN instrument, absence of the impactor, and contributions from aerosol heterogeneity. We note that the inversion approach used in equation (10) differs conceptually from other methods that have been proposed for correcting CCN activation spectra for multiple charge effects [*Frank et al.*, 2006; *King et al.*, 2009; *Rose et al.*, 2008a]. *Rose et al.* [2008a] estimate the fraction of multiply charged particles from the CCN activation curve and subtract this value in their fitting of the activation curve. The method of *Frank et al.* [2006] uses measured size distribution data to estimate the number of multiply charged particles contributing to the activation spectrum. *King et al.* [2009] extended the forward model of *Petters et al.* [2007] to treat cases where hygroscopicity varies with particle size, mobility size is held constant, and supersaturation is varied to measure an activation curve.

[12] In our data processing we first compute $\mathbf{g}_{CCN}$ for the ammonium sulfate calibration runs and the biomass burning smokes. The resulting CCNc response curves are then categorized into four types, as illustrated in Figure 2. Type-I response curves are those obtained from ammonium sulfate aerosol or other pure, sufficiently soluble and hygroscopic single component aerosols. Type-II response curves are continuous activation curves that exhibit a smooth transition between zero and complete activation but are less steep than Type I curves. Type-III response curves exhibit more than one activation mode, consisting of at least one more hygroscopic mode and one less hygroscopic, or nonhygroscopic mode. Type-IV response curves do not exhibit a dominant activation mode. Type-I to -III CCNc response curves were fit to a cumulative Gaussian distribution function

$$f(x) = \frac{1}{2}erfc\left(\frac{x}{\sqrt{2}}\right) \tag{11}$$

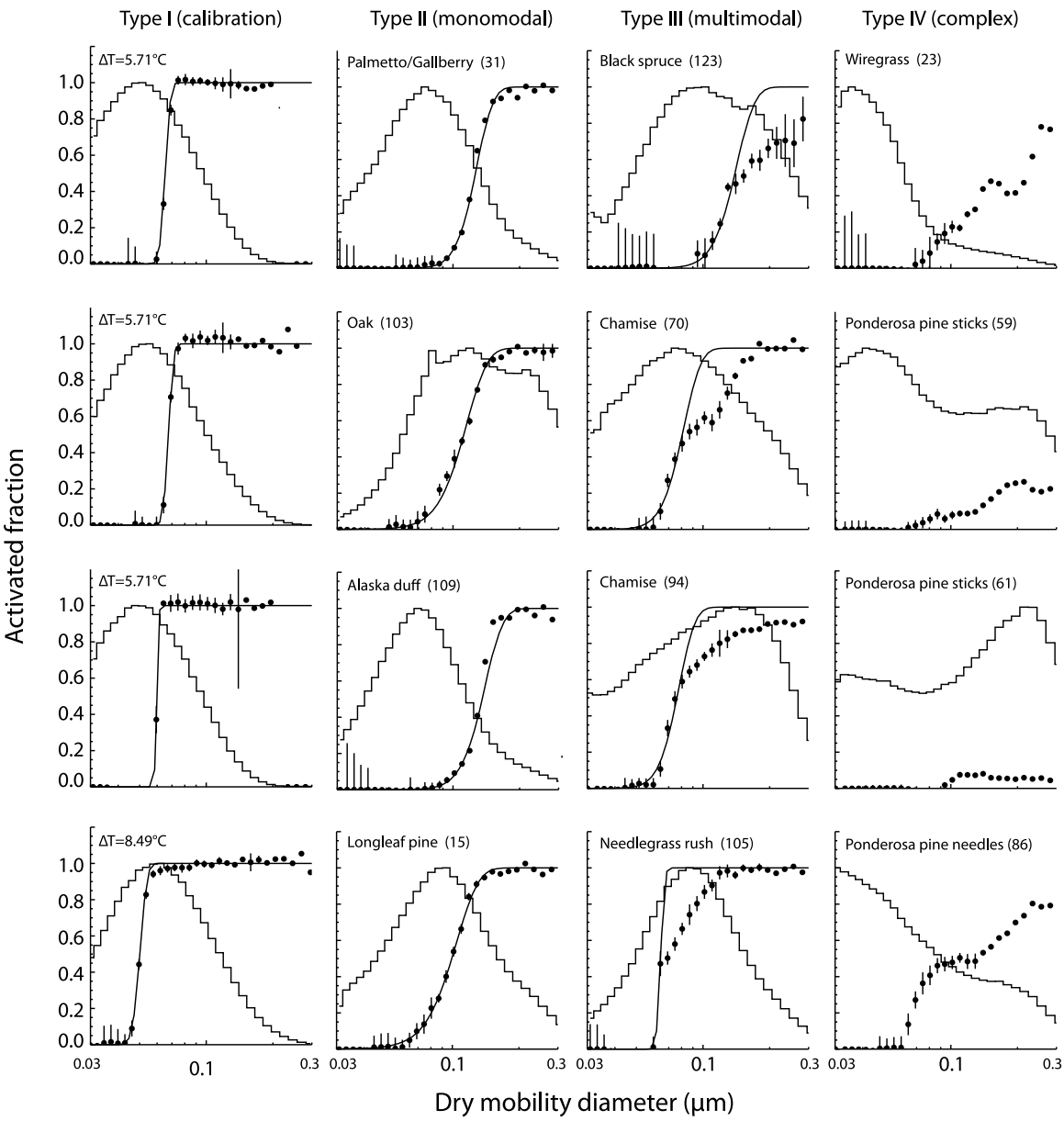

Figure 2. Inverted CCNc response curves (symbols) for a select number of fuels. Vertical bars show ±1 standard deviation from the 30 s sample interval. Solid lines are a cumulative Gaussian distribution fitted to the inverted response curves. Histograms show the underlying normalized particle size distribution. The columns represent the four classification types proposed in this manuscript. The mapping between ΔT and supersaturation is explained in section 2.5.

where x = $(D_d - D_{d,50})/\sigma_D$. In equation (11) erfc is the complementary error function and x is the lower limit of an integral, i.e.

$$erfc(x) = \frac{2}{\sqrt{\pi}} \int_x^\infty \exp(-t^2)dt \qquad (12)$$

In the fitting procedure D_d is the dependent variable and $D_{d,50}$ and σ_D are adjusted to minimize the square of the difference between *f(x)* and the data. $D_{d,50}$ is the dry diameter where $\mathbf{g}_{CCN} = 0.5$ and is interpreted as the diameter where 50% percent of the particles have activated into cloud droplets. We use $D_{d,50}$ as the activation diameter from which we derive κ. We note that CCN-derived κ values imply a certain range of dry diameters for which this value is valid. That range can be calculated from the range of studied supersaturation, and κ values reported here. Instrument supersaturations varied between 0.27 and 0.46% and thus a CCN-derived κ ~0.1 corresponds to activation diameters of 86–120 nm and κ~0.4 to activation diameters of 54–78 nm. Diameter ranges can be calculated for arbitrary κ values using equation (3). Further, σ_D is the CCN response curve width and denotes one standard deviation of a Gaussian distribution. At diameters $D_d - \sigma_D$, and $D_d + \sigma_D$, 16% and 84% of particles have activated into cloud droplets, respectively. Comparing Type I and II

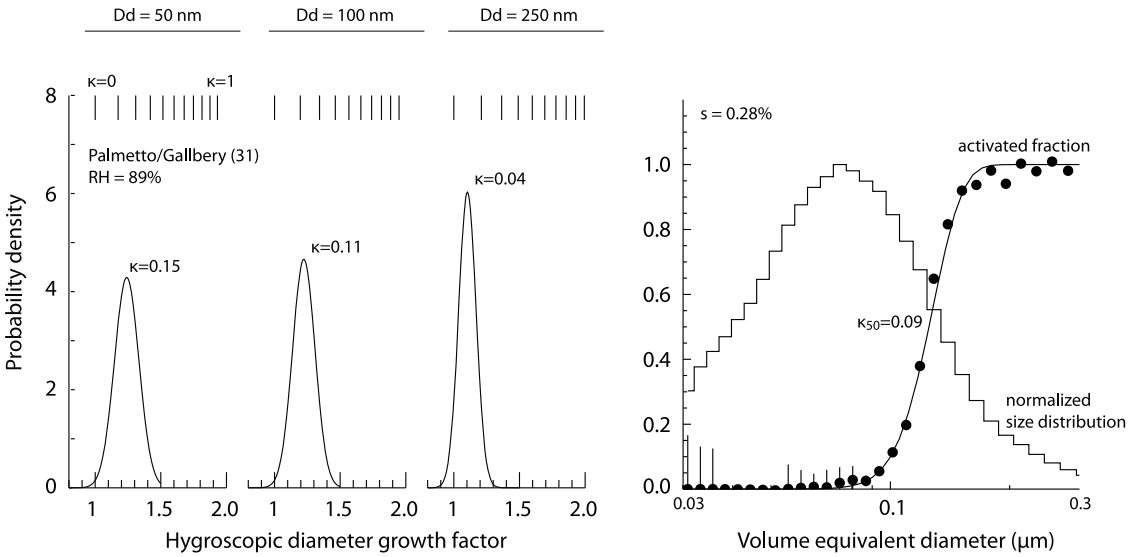

Figure 3. (left) Growth factor probability density functions (GF-PDF) for 50, 100, and 250 nm dry diameter particles at RH = 89% for the palmetto (leaves)/gallberry (leaves + stems) smoke sample. The vertical tick marks located above the GF-PDFs indicate the relationship between wet diameter and κ at the sampling relative humidity. (right) Type-II CCNc response curve (also shown in Figure 2).

spectra reveals that σ_D differs between these two types and this difference is due to the degree of sample heterogeneity. We note that our characterization of CCN activation spectra is very similar to the approaches of *Rose et al.* [2008b] and *Gunthe et al.* [2009] who also use equation (11) but with a variable prefactor that allows fitting Type-III activation curves, where the activated fraction plateaus at a value that is different from unity.

[13] If the size distribution consists of internally mixed particles that have identical composition, and solution surface tension is not a function of particle size, $\mathbf{g}_{CCN}$ reduces to the CCNc transfer function. Ammonium sulfate calibration particles nearly satisfy this criterion. Therefore the fitted inverted activation curves in the left column of Figure 2 are a direct measure of the resolution that can be achieved using our experimental setup. We express the relative width of the response curves as $\beta_{CCN} = \sigma_D/D_{d,50}$ [see also *Rose et al.*, 2008b], which are the fitted parameters in equation (11). Because β_{CCN} is the ratio $\sigma_D/D_{d,50}$ it expresses the width of the activation spectrum in log D_d space as shown in Figure 2. Larger values of β_{CCN} correspond to a broader span between the 16 and 84% fractions of activation. For ammonium sulfate $\beta_{CCN} = 0.05 \pm 0.02$ (n = 16). This value has contributions from residual errors in the inversion because we did not account for measurement errors in this procedure (i.e., $\varepsilon_i = 0$ in equation 15) and nonideal transfer through the CCNc instrument.

[14] For the Type-II spectra $\beta_{CCN} = 0.15 \pm 0.07$ (n = 79). Thus the smokes exhibit a three times broader activation behavior, on average, than what is expected from the technique alone. We attribute this behavior to chemical heterogeneity. Scanning electron microscope images of biomass burning particles produced by similar methods and in the same laboratory reveal a myriad of shapes and compositions, ranging from spherical oily particles, to crystalline cubes and agglomerated soot structures [*Chakrabarty et al.*, 2006; *Hopkins et al.*, 2007]. Distributions of particle shape also contribute to increased values of β_{CCN} because, at any given mobility diameter, particles with different shape factors, but identical chemical composition, will have different dry volume equivalent diameters [*Carrico et al.*, 2008]. This will lead to a range of different activation diameters for the same particle size and hence results in the broadening of the activation curve. In summary, β_{CCN} represents a measure of nonideality in the experimental setup for homogeneous calibration aerosol and values of β_{CCN} that exceed the calibration benchmark are a measure of sample heterogeneity for Type-II activation spectra. Thus β_{CCN} may provide additional insights about the composition of the sampled aerosol that go beyond the average reported hygroscopicity.

3. Results and Discussion

3.1. Burn Data

[15] Figure 3 shows size-resolved growth factor data and the corresponding CCN activation spectrum for emissions from the combustion of a mixture of palmetto leaves and gallberry leaves and stems. The corresponding CCN activation spectrum (right plot) is a monomodal Type-II activation spectrum with $D_{d,50}$ = 136 nm, corresponding to $\kappa_{CCN} \sim 0.09$. The plots in the left panels show the growth factor probability density functions (GF-PDF) [*Gysel et al.*, 2009; *Swietliki et al.*, 2008] obtained from the *Zhou et al.* [2002] implementation of the TDMA inversion. This inversion method assumes a Gaussian distribution of growth factors and calculates a predicted observed humidified size distribution by accounting for the instrument transfer function and charge correction. Three fitted parameters, the arithmetic mean diameter growth factor, the diameter growth dispersion factor, and the relative number of particles (number fraction) define the GF-PDF for a distinct growth factor mode [*Zhou et al.*, 2002]. To produce the inversion results shown in Figure 3, a monomodal repre-

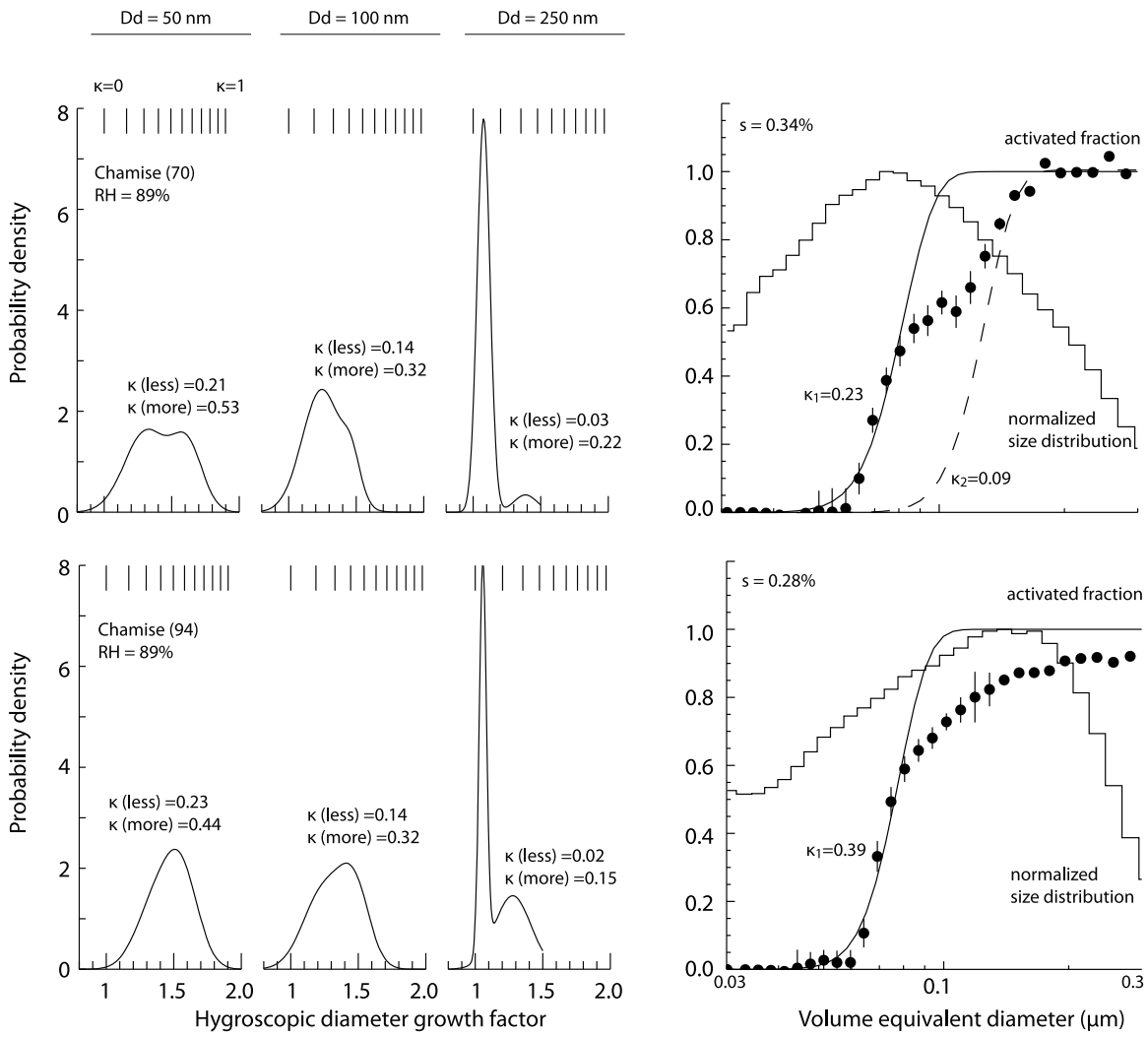

Figure 4. Same as Figure 3 but featuring two chamise burns with Type-III activation spectra.

sentation of the data was selected and the inverted GF-PDF's are plotted for three dry diameters, 50, 100, and 250 nm. The spread factor of the GF-PDF's, defined as standard deviation divided by the mean growth factor, are relatively small (0.06–0.08), but larger than the values obtained at similar humidities for a monodisperse single compound aerosol such as ammonium sulfate (0.02–0.04). This indicates that particles in the selected mobility size cut have similar hygroscopicities. Despite this homogeneity within a single size cut, the 50 nm diameter particles are slightly more hygroscopic than the 100 nm diameter particles, which are substantially more hygroscopic than the 250 nm diameter particles. The best fit κ decreases with size from $\sim$0.15 (D_d = 50 nm) to 0.04 (D_d = 250 nm). In this analysis we assume that particles are in thermodynamic equilibrium. At our residence time of $\sim$5 s particles may not have reached equilibrium and thus the difference in observed κ values at different sizes may reflect a kinetic effect, where the smaller sizes are closer to the equilibrium wet diameter than the larger particles and thus would have an apparently larger κ value [e.g., *Sjogren et al.*, 2007]. Another possibility is that the wetting/drying cycle during the sample preconditioning is not completely efficient, such that larger particles are less spherical than smaller ones, resulting in lower measured growth factors and an apparently reduced hygroscopicity. However, we believe that the observed decrease in κ is at least in part due to true compositional differences at different sizes, as will be discussed later. Although the decrease of κ with size complicates the comparison between HTDMA-derived and CCN-derived hygroscopicity, the HTDMA-derived κ ($\kappa_{\mathrm{HTDMA,\ Dd\ =\ 100\ nm}}$ = 0.11) of the particle diameter closest to $D_{d,50}$ is consistent with the CCN-derived κ = 0.09. This comparison is more complicated for the Type-III spectra, as illustrated in Figure 4, where we present the same type of data for emissions from two chamise plant burns.

[16] We first discuss the result from burn 70 shown in the top plots in Figure 4. The bimodal structure of the GF-PDF for D_d = 50 nm suggests the presence of at least two particle types having different hygroscopicities. The inversion algorithm by *Zhou et al.* [2002] was setup to retrieve more and less hygroscopic modes. For the D_d = 100 nm particles the humidified size distribution also suggests that multiple particle types were present. These modes, however, cannot always be resolved visually and the inversion algorithm can selectively compute either an average single mode or bimodal GF-PDF. Particles with D_d = 250 nm generated from the chamise burn were only weakly hygroscopic,

similar to the 250 nm diameter particles produced by the palmetto (leaves)/gallberry (leaves + stems) mixture (Figure 3). The CCN activation curve for the chamise smoke was expected to have a more complex structure than that for the palmetto (leaves)/gallberry (leaves + stems) mixture, because the chamise emissions contained more than one particle type, as shown by the HTDMA data. For the CCN scan at s = 0.34%, two distinct activation modes are apparent, corresponding to a Type-III activation spectrum. The first mode displays a sharp increase at D_d = 70 nm, corresponding to $\kappa_{CCN} \sim 0.23$. This value is consistent with the growth factor data at D_d = 50 nm and D_d = 100 nm, which suggest that the activation diameter at the instrumental supersaturation should range from 63 nm (κ = 0.48) to 90 nm (κ = 0.16). At larger sizes the hygroscopicity is lower but sufficient to activate all particles larger than about $D_d \sim$ 150 nm at the selected s = 0.34%. This second mode, with κ_{CCN} = 0.09, falls within the range of κ determined using the HTDMA for 100 and 250 nm particles. We note that the CCN activation spectrum represents a continuous distribution of κ values. Consequently, the fitted error functions from which κ_{CCN} = 0.09 and 0.23 were evaluated are to some extent arbitrary and should be interpreted as approximate bounding values for CCN-derived κ values in the 50–100 nm diameter range.

[17] Figure 4 also shows activation and growth curves from a replicate burn of chamise (burn 94). By comparing the growth factor data it appears that the two burns produced smoke with similar chemical composition and heterogeneity. Both samples have the same strong decrease in κ values between the 50 and 250 nm particles and both have broadened GF-PDF's, indicating heterogeneity in composition at a single mobility size. In the CCNc response curve, the fit of the error function suggests κ_1 = 0.39 for D_d ~60 nm particles and this value constrains the maximum expected κ for the more hygroscopic tail of the underlying asymmetric κ distribution. The activated fraction does not approach unity, suggesting that 10% of particles did not activate at 300 nm and s = 0.28%, and have a corresponding hygroscopicity of $\kappa < \sim 0.01$. The 10% fraction of particles with $\kappa < \sim 0.01$ at D_d = 300 nm that did not activate, and the 90% of particles with $\kappa > \sim 0.01$ at D_d = 300 nm that did activate in the CCN instrument cannot be resolved separately in the GF-PDF measured by the HTDMA for the D_d = 250 nm distribution.

[18] The particle size distribution, chemical composition, and resulting heterogeneity of the smoke emissions are governed by several processes, including soot generation during the flaming fire phase, high temperature volatilization and condensation of inorganic compounds, and coagulation and condensation of low volatility hydrocarbons that are released during the smoldering fire phase [*Reid and Hobbs*, 1998]. The important role of inorganic compounds for promoting CCN activity of biomass burning aerosol was already noted by *Rogers et al.* [1991]. Electron microscopy of ambient smoke samples shows that the most common particle type is sub-100 nm organic particles with inhomogeneous inorganic inclusions that vary with the age of the smoke and the type of burned vegetation [*Posfai et al.*, 2003]. Chamise, when burned, releases relatively large number concentrations of sub-100-nm diameter hygroscopic particles, which can be deduced from the number size distribution and the measured growth factors (Figure 4). These particles have κ values substantially larger than expected for pure organic compounds but smaller than for pure inorganic compounds, suggesting that these particles are qualitatively consistent with the particles analyzed by Posfai et al. Simultaneously, larger, i.e., >100 nm diameter, chain aggregates of soot spherules are emitted. Individual soot spherules 20–40 nm in diameter form in the flame, probably via a polymerization reaction. Rapid agglomeration occurs in the flame and upon exiting the flame zone of the fire, producing larger chain aggregates [*Moosmüller et al.*, 2009]. As the plume cools further and dilutes, the chain aggregates become coated with organic compounds that condense onto them. Such mixed particles are likely candidates for the larger, almost nonhygroscopic ($\kappa \sim 0$) seen by the HTDMA and CCNc. With time, the different particle types coagulate and lead to even more complicated mixtures. During the stack burns the initial particle number concentrations (D > 5 nm) in the drum often exceeded 500,000 cm^{-3}. Under those conditions coagulation occurs on a time scale of minutes and the extent to which coagulation mixes various particles types will influence the measured hygroscopicity. If this conceptual view is correct, the extent to which multiple growth modes are observable in the HTDMA and CCNc, and as a result the reported range of the κ values, depends on the duration of the flaming/smoldering phase, the fire temperature, total aerosol number concentration and rapidity of dilution, extent of organic coatings, and elapsed time between emissions and sampling.

[19] We summarize the hygroscopicity parameters for the Type-II (open symbols) and Type-III spectra (closed symbols) as functions of fuel type in Figure 5. In case of the Type-III spectra the plotted κ value only represents the more hygroscopic mode. In Figure 5 we also differentiate between stack burns (black) and chamber burns (red), which differ in the age and the dilution history of the smoke. Before discussing the figure in detail we point out that the particle composition heterogeneity produced by the emission processes, and burn-to-burn differences in the emissions, make it difficult to assign a single κ value that is representative of the emissions from the burning of each fuel. Despite the confounding effects of sample heterogeneity, a single approximate hygroscopicity parameter can be assigned for some of the smokes, particularly those with lower hygroscopicities. Examples include smoke emissions from ponderosa or longleaf pine needles and sticks, Douglas fir needles and branches, and smoldering duff core. These smokes were well characterized by a range of $0.05 < \kappa < 0.19$, as indicated by the gray shading in the figure. Bulk chemical analyses show that these smokes are dominated by organic carbon [*McMeeking et al.*, 2009]. We note that this range is similar to the range of κ values which has been observed for secondary organic aerosol in chamber experiments ($0.06 < \kappa < 0.14$) [*Duplissy et al.*, 2008; *King et al.*, 2009; *Prenni et al.*, 2007] and also in the range of estimates for the organic component of ambient aerosol ($0.02 < \kappa_{organic} < 0.2$) [*Carrico et al.*, 2005; *Gunthe et al.*, 2009; *Shantz et al.*, 2008; *Wang et al.*, 2008].

[20] Much more variability in κ was seen for the more hygroscopic smokes. The increased presence of filled symbols from Type III spectra above the gray shaded area

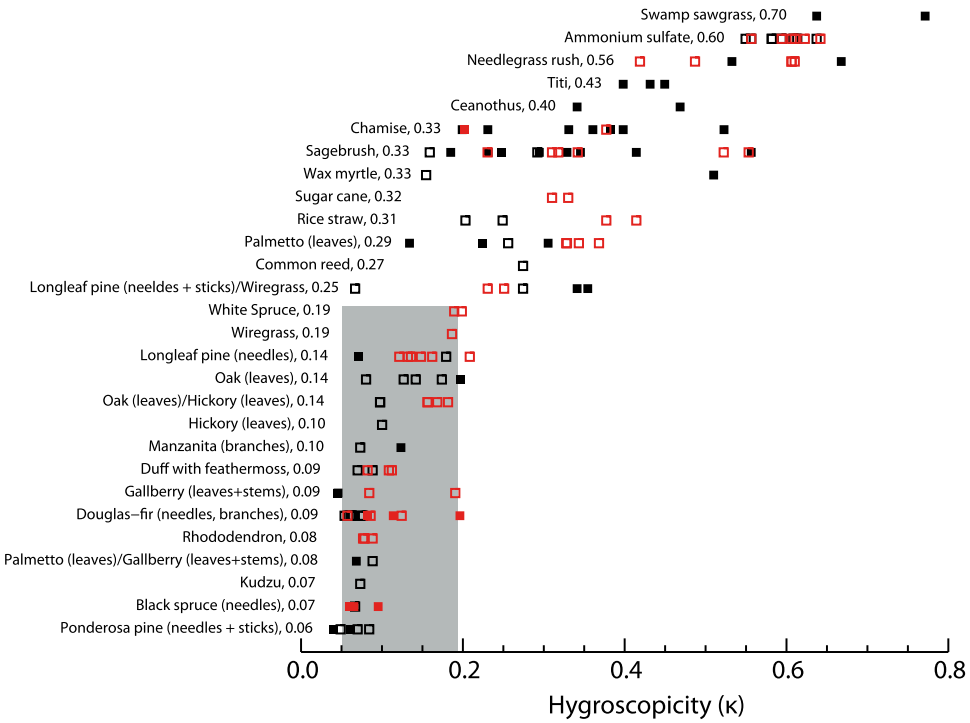

Figure 5. Ranked hygroscopicity parameters inferred from the CCN activation data. Open symbols are Type-I and Type-II spectra; solid symbols are Type-III spectra, and only the more hygroscopic mode is charted; black symbols are stack burns; and red symbols are chamber burns. Numbers behind the common name indicate the average κ value derived from multiple burns. The observed range in ammonium sulfate values is explained in section 2.5. Unless noted in parentheses, the entire plant was burned. Plant names and locations of sampling are given in Table 1.

indicates that those burns were more likely to produce externally mixed heterogeneous particles (see also Figure 4), and also that multiple burns of the same fuel produced a wide range of hygroscopicity values. For example, for both stack and chamber burns, interburn variability for sagebrush smoke emissions resulted in a range of $\sim 0.1 < \kappa < \sim 0.6$. In a companion paper, we show that whereas many carbon-dominated smokes exhibited κ near 0.1, as discussed above, increasing mass fractions of inorganic species resulted in the emergence of a second, more hygroscopic mode (C. M. Carrico et al., manuscript in preparation, 2009).

3.2. Conceptual Model of the CCN Activity for Biomass Smoke

[21] The summary in Figure 5 neither accounts for sample heterogeneity (Figures 3 and 4) nor for particle size effects on CCN activity. To integrate our experimental results (size, hygroscopicity, and chemical heterogeneity) we use a three-component model to conceptualize CCN emissions from the fires. The three components are hygroscopic inorganic compounds, organic carbon, and components such as elemental carbon [*Dusek et al.*, 2006] or long chain hydrocarbons that do not contain polar functional groups [*Petters et al.*, 2006]. The latter compounds are likely well modeled as $\kappa \sim 0$ in mixtures containing some fraction of hygroscopic material, but unmixed soot particles may require higher supersaturations for activation than those predicted by $\kappa = 0$, due to their complex shapes and wetting contact angle [*Fletcher*, 1958; *Mahata and Alofs*, 1975; *Raymond and Pandis*, 2002]. We use our data to assign numerical values for representative dry diameters and hygroscopicities for each of the three components, and then translate those into critical supersaturation-dry diameter space to analyze their CCN activity (Figure 6).

3.2.1. Inorganic Emissions

[22] The only smokes which exhibit $\kappa > 0.6$ in the CCN measurements, indicative of the presence of inorganic compounds [*Petters and Kreidenweis*, 2007], were those in which the activation diameter did not exceed 50 nm. Further, the growth factor data for D_d = 50 nm and D_d = 100 nm (Figures 3 and 4) (Carrico et al., manuscript in preparation, 2009) suggest that hygroscopic particles with $\kappa < 0.6$ are most often emitted by fires at those sizes. κ values <0.6 suggest that if inorganic compounds are present, they are likely to be internally mixed with carbonaceous compounds that serve to reduce the mixture κ. We assign the inorganic component a κ value of 0.6 which serves as a lower estimate of inorganic compound hygroscopicity; assume that, if this inorganic particle is unmixed with other species, its size does not exceed 50 nm; and assume that, if it becomes mixed with other species, the inorganic core of such mixed organic/inorganic particles does not exceed 50 nm.

3.2.2. Soot Emissions

[23] At the other end of the hygroscopicity spectrum is the nonhygroscopic mode. As shown in Figures 3 and 4, hygroscopicity generally decreased with increasing size. At D_d = 250 nm, κ values near zero are were often observed in the HTDMA, and some fraction of larger particles did not activate into cloud droplets, even at 300 nm (Figure 4). Combined, these observations suggest that the nonhygro-

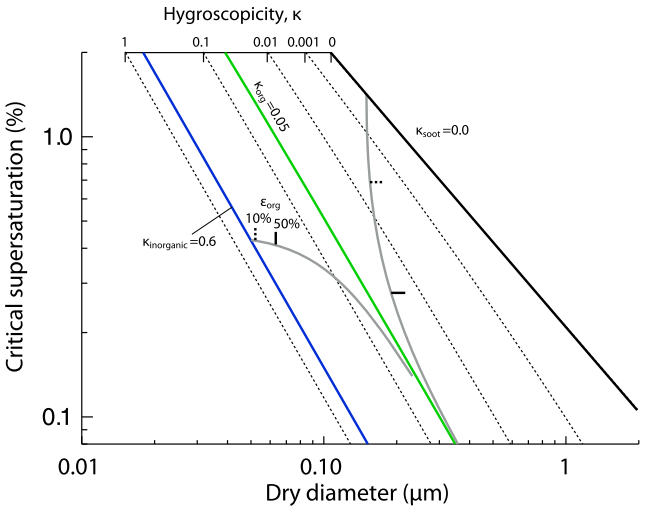

Figure 6. Illustration of CCN activity for several particle types. Blue denotes inorganic particles with assumed $\kappa = 0.6$. Green denotes organic particles with assumed $\kappa = 0.05$. Black denotes assumed nonhygroscopic particles with $\kappa = 0$. Gray denotes mixed inorganic-organic or nonhygroscopic-organic particle types with variable volume fractions, ε_{org}. For construction of the gray lines, a single size is assumed for the inorganic core (50 nm) and the nonhygroscopic core (150 nm) before organic coating is applied in the model. Dashed and solid tick marks on the mixing lines denote $\varepsilon_{org} = 0.1$ and 0.5, respectively.

scopic fraction was dominated by larger particles. SEM images from chamise smoke [*Chakrabarty et al.*, 2006; *Lewis et al.*, 2009] indicate that these may be large, fractal-like particles. For the purposes of the following discussion, we assume that a certain fraction of emitted particles is nonhygroscopic ($\kappa = 0$) and that this component has a characteristic diameter $D_d = 150$ nm.

3.2.3. Organic Carbon Emissions

[24] The third component in our model is organic carbon, which on a mass fractional basis was the most abundant aerosol component emitted during the burns [*McMeeking et al.*, 2009]. Although we do not know the hygroscopicity of the individual organic compounds, we assign $\kappa_{organic} = 0.05$ based on the lower limit of CCN-derived hygroscopicity for the organic dominated fuels (Figure 5). We choose this value to reflect a lower reasonable estimate of its effect on CCN activity. A similar lower limit estimate can be derived from the HTDMA data. Due to its abundance, we assume that particles dominated in composition by organic carbon can be present at all sizes ($30 < D_d < 300$ nm).

[25] Figure 6 illustrates the relationship between dry diameter and critical supersaturation with lines of constant κ superimposed. These lines are calculated by specifying an array of dry diameters, fixing κ and computing the corresponding s_c using equation (3). Supersaturations in excess of 0.2% are necessary for particles to serve as CCN at the sizes and hygroscopicities that they are emitted from fires ($D_d < 300$ nm, $\kappa > 0.05$). However, Figure 6 demonstrates that at 1% supersaturation particles with $\kappa = 0.05$ and $D_d > 65$ nm activate. In our experiments, the number mode of emissions ranged from 60 to 200 nm (Figure 2) and thus the conceptual model suggests that majority of the emitted aerosol form cloud droplets between 0.2 and 1% supersaturation, even if they have low κ characteristic of the organic component (0.05). We recall that $\kappa \sim 0.05$ reflects a lower estimate of organic aerosol hygroscopicity and increased values imply lower activation supersaturations for the same particle dry diameter. The range of CCN activity for the particles discussed here compares to that of Aitken mode (mode diameters 30–80 nm) pure ammonium sulfate particles. The inorganic cores, even though they are emitted at smaller sizes, are also CCN active under those conditions because of their higher κ. Similarly, despite their low hygroscopicity, particles that have $\kappa \sim 0$ can serve as CCN, if they are emitted at sufficiently large sizes ($D_d >$ 200 nm). This simple conceptual analysis suggests that most submicron particles emitted in open biomass combustion activate between 0.2% and 1% supersaturation. If true, then aging of biomass emissions from hydrophobic-to-hydrophilic, as is assumed to be necessary in some global models, is not required to produce CCN-active particles from biomass burning. However, as can be seen from Figure 6, only the largest particles ($D_d > 300$, $\kappa \sim 0.05$) will be able to serve as droplet nuclei in cloud regimes where peak supersaturations are limited to values less than 0.2% (e.g., fogs and stratus). Since the number concentrations of such larger particles emitted in our experiments are low, this implies that particles derived from biomass burning cannot compete with more abundant ambient particles to nucleate cloud droplets under low peak supersaturation conditions. However, as particles evolve in an aging plume they grow via coagulation or condensation of secondary inorganic compounds, such as NH_3, H_2SO_4, and HNO_3, they may also become sufficiently active to participate in cloud droplet formation in these low peak supersaturation cloud regimes [*Chand et al.*, 2005].

[26] In the concentrated environment of a fresh smoke plume, both the inorganic and the nonhygroscopic particles can quickly become coated with the moderately hygroscopic ($\kappa \sim 0.05$) organic compounds. Soot particles are also often found in complex mixing states consisting of soot, inorganic, and organic compounds [*Lewis et al.*, 2009]. The hygroscopicity of a mixed particle can be described using the following mixing rule [*Petters and Kreidenweis*, 2007]

$$\kappa_{mixture} = \varepsilon_{org}\kappa_{org} + \left(1 - \varepsilon_{org}\right)\kappa_{core} \tag{13}$$

where $\kappa_{mixture}$ is the hygroscopicity of the mixed particle, ε_{org} is organic volume fraction, κ_{org} the hygroscopicity of the organic compound, and κ_{core} the hygroscopicity of the compound the organic is condensing on. Equation (13) is written for two-component aerosol to simplify the following discussion, but is valid for any number of components. Assuming a value for κ_{core} and starting at a specified dry diameter where the contribution of organic carbon is assumed to be zero, it is possible to compute mixing lines in s_c–D_{dry} space. Two examples are depicted by the gray lines in Figure 6. Our inorganic-organic mixing scenario starts with $D_d = 50$ nm and $\kappa_{core} = 0.6$. Then a specified amount of organic volume is added to the particle, determining $\kappa_{mixture}$ using equation (13) and a modified dry diameter calculated assuming zero volume change due

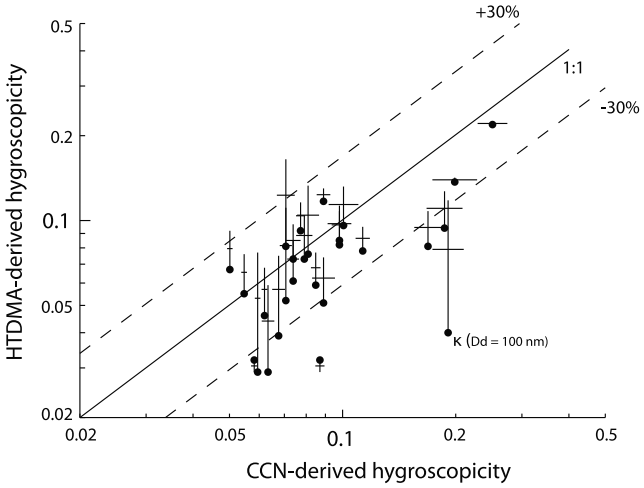

Figure 7. Comparison between HTDMA-derived and CCN-derived hygroscopicity values (κ). Symbols denote HTDMA-derived κ values corresponding to D_d = 100 nm for samples with only one growth mode in the HTDMA. The vertical lines indicate the range of HTDMA-derived κ values due to size dependence and the upper limit indicates the κ values for D_d = 50 nm. The horizontal lines indicate the expected range in CCN-derived κ values based on the width of the CCNc response function. Only Type-II CCN response functions are included in the comparison.

to mixing. Using $\kappa_{mixture}$ and the modified dry diameter, the critical supersaturation is calculated. As one would expect, the mixed particle CCN activity is similar to that of the organic particles if the organic volume fraction becomes large, causing the mixing line to converge with the assumed κ_{org} isoline. Mixing an inorganic particle with condensed organic matter decreases the effective κ of the particle, while the particle diameter increases. The diameter increase lowers critical supersaturation more effectively than the reduced κ increases it, and thus the process of condensation of the organic onto the core inorganic particles will overall decrease the critical supersaturation required to activate the particle: hence, the organic coating increases the CCN activity (decreases critical supersaturation) of the original, highly hygroscopic inorganic particle. Our nonhygroscopic organic mixing scenario starts with D_d = 150 nm and κ = 0. Any condensation of a component with $\kappa > 0$ increases both particle size and hygroscopicity, and thus even small fractional additions of organic are seen to strongly decrease the critical supersaturation of the particle. The critical supersaturation of initially nonhygroscopic cores (κ = 0) decreases significantly more than in the case of initially inorganic hygroscopic cores (κ = 0.6) for the same volume of organic material (κ = 0.05) condensed on to the core.

[27] The foregoing discussion is intended to serve as an illustrative set of examples that can easily be extended to three or more hygroscopicity classes. The presence of a third component will complicate the illustration shown in Figure 6, although a particle's critical supersaturation will always decrease when compounds with $\kappa > 0$ are mixed with a pre-existing core having arbitrary hygroscopicity. However, it is important to draw a clear distinction between our conceptual model, which integrates HTDMA, CCN and composition measurements, and the directly measured critical supersaturations. The CCN data in Figure 5 are for instrument supersaturations 0.27–0.46%. To explore the full range of supersaturations shown in Figure 6, the integrated measurements have been used to extrapolate outside this supersaturation range.

3.3. Hygroscopic Growth Versus CCN-Derived Hygroscopicity

[28] As discussed on the basis of the individual burn examples, a comparison between *gf*-derived κ and CCN-derived κ is complicated by sample heterogeneity. Nevertheless, Figures 3 and 4 demonstrate that the two measurements do yield self-consistent results when compared in the appropriate size range. In the following analysis we restrict ourselves to burns exhibiting Type-II CCN response functions, i.e., monomodal functions with less heterogeneous emissions. Further, we only consider samples with HTDMA-derived κ values that are well fit using a single hygroscopic mode using the TDMA inversion routine, again eliminating the most heterogeneous samples. The scatter diagram for the remaining burns is shown in Figure 7. The filled symbols show the growth factor derived κ values for D_d = 100 nm, most appropriate for the comparison with the CCN activation spectra for the low-κ fuels (Figure 3). This point is connected to the hygroscopicity value derived at D_d = 50 nm by the vertical bar and thus this bar depicts the range in hygroscopicity in the 50–100 nm size range. The CCN-derived κ value is obtained from the 50% activation point (Figure 3). Heterogeneity in CCN-derived values is plotted as the κ value that would be derived from the 16% and 84% activation diameters respectively, and this range was measured using the quantity β_{CCN}. The data demonstrate that the derived κ values are generally consistent within ±30%. The smoke particles do not exhibit the marked discrepancies between subsaturated and supersaturated hygroscopicity values that have been observed for some secondary organic aerosols or aerosol water extracts [*Prenni et al.*, 2007; *Ziese et al.*, 2008]. The origin of this discrepancy for the secondary organic aerosols is not fully understood but surface tension effects, gradual dissolution of sparingly soluble compounds, or degree of oxygenation of the organics all seem to play a role [*Petters et al.*, 2009b]. The fact that no discrepancy is observed for the biomass burning organic compounds suggests that these organics behave similarly to oxygenated organics such as sugars, carboxylic acids [*Chan et al.*, 2008] or oxygenated high molecular weight compounds such as humic acid and polyacrylic acid [*Petters and Kreidenweis*, 2007] where HTDMA-derived and CCN-derived κ values are in reasonable agreement.

4. Summary and Conclusions

[29] Fresh biomass burning emissions have complex hygroscopic behavior. Individual activation spectra show that smokes are generally externally mixed, that hygroscopicity generally decreases with particle size, and that more and less hygroscopic modes are frequently observed at a single size. This behavior complicates size-resolved CCN measurements and the correct removal of multiply charged particle effects. The inversion scheme we propose provides

a first order correction of activation spectra that is not dependent on aerosol mixing state. The broadness of the inverted activation spectrum can be used to characterize the heterogeneity of the sample. Limiting the comparison to the more homogeneous cases, closure between hygroscopic growth factor derived and CCN derived hygroscopicity was achieved within ±30%. This closure is noteworthy particularly for the organic carbon dominated smokes, which is in contrast to the behavior of SOA generated inside smog chambers, suggesting the biomass burning derived organic carbon is substantially different in composition from first generation SOA products. One likely difference is the degree of oxygenation which may cause HTDMA- and CCN-derived κ values to diverge substantially [*Petters et al.*, 2009b]. H-NMR analysis suggests that ambient biomass burning derived water-soluble organic carbon is more oxygenated than SOA generated from biogenic volatile organic compounds [*Decesari et al.*, 2007] but it is not clear if this result holds when comparing first generation smog-chamber derived SOA and fresh biomass burning emissions at laboratory scale as is done here. The data reported here show that growth factor data or direct CCN measurement can be used to characterize biomass burning smoke and that each instrument provides a different perspective on the overall composition.

[30] Many of the smokes were heterogeneous in composition and water uptake properties and a single hygroscopicity parameter could not be assigned over the entire size distribution. This is consistent with our general understanding of how fires generate particles [*Reid and Hobbs*, 1998]. Nevertheless, these data apply to fresh emissions and some of the complexity may be averaged out by coagulation and coating of particles with secondary compounds downwind. Ambient measurements of biomass burning affected air masses suggest that these particles have $0.1 < \kappa < 0.4$, and that value is only weakly dependent on the aerosol size distribution [*Carrico et al.*, 2005; *Rose et al.*, 2008b]. Conceptually separating the emissions into inorganic, organic, and elemental carbon emissions, and accounting for the size dependence of each fraction, showed that most of the particles in our open burning experiments could serve as CCN in vigorous cumulus updrafts. A conversion from hydrophobic-to-hydrophilic via chemical aging or condensation of secondary inorganic compounds is not required for these particles to be active under these conditions.

[31] Plants that thrive in saline soils compartmentalize the extra solutes in their tissues to cope with salt-induced stress on osmoregulation, ion toxicity, and nutrient balance [*Gorham et al.*, 1985], and thus contain larger fractions of inorganic substances in their matrices. Biomass burning emission factors of chlorine have been observed to trend linearly with fuel chlorine content [*Christian et al.*, 2003], and it is reasonable to assume that this holds more generally for other inorganic fuel species. We therefore suggest that smokes generated from fuels growing in saline soils produce the most hygroscopic aerosols, at least when fire temperatures are sufficiently high. Unfortunately, no universally accepted database exists that allows for categorizing plant salt tolerance [*Glenn et al.*, 1999] and salt tolerance alone does not ensure high fuel inorganic content. We suggest that future studies should include measurements of plant and soil elemental composition to test the hypothesized link between soil composition, fuel composition, and hygroscopicity of smokes produced when that fuel is burned. Although organic coatings reduce the overall hygroscopicity of inorganic particles, the diameter increases and the combined effects result in an overall increase in the CCN activity of the coated particle.

Appendix A

[32] The inversion problem as written in equation (7) is $\mathbf{R} = \mathbf{A}(\mathbf{g} \circ \mathbf{N})$. The matrix $\mathbf{A}$ is defined by the instrument geometry, DMA transfer function, selected electric potential, and chosen flow rates

$$\begin{bmatrix} R_1 \\ R_2 \\ \vdots \\ R_n \end{bmatrix} = \begin{bmatrix} \sum_{k=1}^{m} K_1(D_{1,k})P_k(D_1) & \sum_{k=1}^{m} K_1(D_{2,k})P_k(D_2) & \cdots & \sum_{k=1}^{m} K_1(D_{n,k})P_k(D_n) \\ \sum_{k=1}^{m} K_2(D_{1,k})P_k(D_1) & \sum_{k=1}^{m} K_2(D_{2,k})P_k(D_2) & \cdots & \sum_{k=1}^{m} K_2(D_{n,k})P_k(D_n) \\ \vdots & \vdots & \ddots & \vdots \\ \sum_{k=1}^{m} K_n(D_{1,k})P_k(D_1) & \sum_{k=1}^{m} K_n(D_{2,k})P_k(D_2) & \cdots & \sum_{k=1}^{m} K_n(D_{n,k})P_k(D_n) \end{bmatrix} \left[\begin{bmatrix} g_1 \\ g_2 \\ \vdots \\ g_n \end{bmatrix} \circ \begin{bmatrix} N_1 \\ N_2 \\ \vdots \\ N_n \end{bmatrix} \right] \tag{A1}$$

The kernel function $K_i(D_{j,k})$ is calculated in a multistep procedure. First the kernel function is determined in electrical mobility (Z) space $K_i(Z_i)$, The mobility centroid, Z_i, of the ith channel for a cylindrical DMA column is [*Knutson and Whitby*, 1975]

$$Z_i = \frac{Q_{sh} + Q_e}{4\pi LV} \ln\left[\frac{R_2}{R_1}\right], \tag{A2}$$

where Q_{sh} is the volumetric sheath flow, Q_e is the volumetric excess flow, L is the length of the DMA column, V is the negative potential applied to the inner cylinder, and R_1 and R_2 are the radial location of the aerosol exit and entrance, respectively. The full-width-half-maximum interval, ΔZ, of the ideal, nonbroadened triangular transfer function is

$$\Delta Z = \frac{Q_a + Q_s}{Q_{sh} + Q_e} Z_i, \tag{A3}$$

where Q_a is the volumetric aerosol flow rate and Q_s is the volumetric sample flow rate. The transfer function, $\Lambda(Z_i)$, is a triangular weighting function. At the centroid mobility, $\Lambda(Z_i) = 1$ and at the full-width-half-max, $\Lambda(Z_i - 0.5\ \Delta Z) = \Lambda(Z_i + 0.5\ \Delta Z) = 0.5$. No transmission occurs beyond the boundaries of $Z^* \pm \Delta Z$, i.e., $\Lambda(Z_i - \Delta Z) = \Lambda(Z_i + \Delta Z) = 0$. Deviations from the triangular transfer function may occur due to well-known sources of broadening such as particle diffusion, nonuniform distribution of the particles in the

inlet, imperfections in the electrode geometry or imperfections of the flow field [*Flagan*, 1999]. Other functional forms for $\Lambda(Z_i)$ can easily be substituted for the form chosen here.

[33] In equation (5) the integral is defined using physical diameter as the independent variable. The conversion from diameter to electrical mobility is

$$Z_{j,k} = \frac{keC_c(D_{j,k})}{3\pi\mu D_{j,k}\chi} \tag{A4}$$

where e is the elementary charge, C_c is the Cunningham slip correction factor, μ is the dynamic viscosity of air, k is the number of elementary charges on the particle, and χ is the dynamic shape factor. Each bin of the inverted size distribution corresponds to a diameter range $[D_{j1,k}, D_{j2,k}]$ where D_{j1} is the lower and D_{j2} the upper bin limit. The kernel function $K_i(D_{i,j})$ is the integral transform of the triangular transfer function and the diameter-to-mobility mapping

$$K_i(D_{j,k}) = \int_{Z_{j1,k}}^{Z_{j2,k}} \Lambda(Z_i) dZ_{j,k} \tag{A5}$$

In equation (A5) the integration limits are determined from the diameter bin limits of the inverted size distribution converted to mobility space using equation (A4). The fraction of particles carrying k charges at charge equilibrium, $P_k(D)$, is calculated according to the *Wiedensohler* [1988] parameterization

$$\log_{10}[P_k(D)] = \sum_{i=0}^{5} a_i(k)(\log_{10} D)^i, \tag{A6}$$

for $k = +1$ and $+2$ and where $a_i(k)$ are fitted coefficients which we obtained from the most recent DMA (TSI 3081) manual and for $k > +2$,

$$\ln[f(D, k > +3)] = \ln\left[\frac{e}{\sqrt{4\pi^2\varepsilon_0 D k_0 T}}\right] - \frac{\left(k - \frac{2\pi\varepsilon_0 D k_0 T}{e^2}\ln[r]\right)^2}{\frac{4\pi\varepsilon_0 D k_0 T}{e^2}} \tag{A7}$$

where, k_0 is Boltzmann's constant, ε_0 is the dielectric constant and $r = 0.875$ is the ion mobility ratio. Using equations (A1)–(A7) the inversion matrix **A** can be calculated numerically.

[34] **Acknowledgments.** We acknowledge funding from the Joint Fire Science Program under project JFSP 05-3-1-06. We also acknowledge support from the Department of Energy NICCR under grant MPC35TA-A, the National Aeronautics and Space Administration under grants NNG06F00G and NNG04GR44G, and the National Science Foundation under grant NSF ATM-0521643. We are grateful to Don Collins for suggesting use of standard DMA inversion techniques to interpret CCN activation spectra. We thank Wei-Min Hao and Bill Malm for their key roles in organizing the FLAME study. We thank all supporting members of the FLAME-II team, particularly staff at the USDA Forest Service Fire Sciences Laboratory in Missoula. We thank Amy Sullivan at CSU and the IMPROVE team at UC Davis for aerosol composition measurements. We thank Mike Chandler, Joey Chong, Guenter Engling, Eric Garrell, Grizelle Gonzales, Sue Grace, Jennifer Hinkley, Randi Jant, Sheah Mucci, Rachael Moore, Robert Olson, Kenneth Outcalt, Jim Reardon, Kevin Robertson, Pauline Spain, and David Weise for collecting the fuel samples for the project. We thank Ryan Sullivan for reviewing an early draft of this manuscript. Finally, we thank Ulrich Pöschl and an anonymous reviewer who helped us to significantly improve this manuscript.

References

Alofs, D. J., and P. Balakumar (1982), Inversion to obtain aerosol size distributions from measurements with a differential mobility analyzer, *J. Aerosol Sci.*, *13*(6), 513–527, doi:10.1016/0021-8502(82)90017-9.

Andreae, M. O., D. Rosenfeld, P. Artaxo, A. A. Costa, G. P. Frank, K. M. Longo, and M. A. F. Silvia-Dias (2004), Smoking rain clouds over the Amazon, *Science*, *303*, 1337–1342, doi:10.1126/science.1092779.

Bowman, D. M. J. S., et al. (2009), Fire in the Earth System, *Science*, *324*, 481–484, doi:10.1126/science.1163886.

Carrico, C. M., S. M. Kreidenweis, W. C. Malm, D. E. Day, T. Lee, J. Carrillo, G. R. McMeeking, and J. L. Collett (2005), Hygroscopic growth behavior of a carbon-dominated aerosol in Yosemite National Park, *Atmos. Environ.*, *39*(8), 1393–1404, doi:10.1016/j.atmosenv.2004.11.029.

Carrico, C. M., M. D. Petters, S. M. Kreidenweis, J. L. Collett, G. Engling, and W. C. Malm (2008), Aerosol hygroscopicity and cloud droplet activation of extracts of filters from biomass burning experiments, *J. Geophys. Res.*, *113*, D08206, doi:10.1029/2007JD009274.

Chakrabarty, R. K., H. Moosmüller, M. A. Garro, W. P. Arnott, J. Walker, R. A. Susott, R. E. Babbitt, C. E. Wold, E. N. Lincoln, and W. M. Hao (2006), Emissions from the laboratory combustion of wildland fuels: Particle morphology and size, *J. Geophys. Res.*, *111*, D07204, doi:10.1029/2005JD006659.

Chan, M. N., S. M. Kreidenweis, and C. K. Chan (2008), Measurements of the hygroscopic and deliquescence properties of organic compounds of different solubilities in water and their relationship with cloud condensation nuclei activities, *Environ. Sci. Technol.*, *42*, 3602–3608, doi:10.1021/es7023252.

Chand, D., O. Schmid, P. Gwaze, R. S. Parmar, G. Helas, K. Zeromskiene, A. Wiedensohler, A. Massling, and M. O. Andreae (2005), Laboratory measurements of smoke optical properties from the burning of Indonesian peat and other types of biomass, *Geophys. Res. Lett.*, *32*, L12819, doi:10.1029/2005GL022678.

Christian, T. J. B., R. J. Kleiss, R. J. Yokelson, R. Holzinger, P. J. Crutzen, W. M. Hao, B. H. Saharjo, and D. E. Ward (2003), Comprehensive laboratory measurements of biomass burning emissions: 1. Emissions from Indonesian, African, and other fuels, *J. Geophys. Res.*, *108*(D23), 4719, doi:10.1029/2003JD003704.

Clegg, S. L., P. Brimblecombe, and A. S. Wexler (1998), Thermodynamic model of the system H^+-NH_4^+-Na^+-SO_4^{2-}-NO_3^--Cl^--H_2O at 298.15 K, *J. Phys. Chem.*, *102*(12), 2155–2171.

Collins, D. R., R. C. Flagan, and J. H. Seinfeld (2002), Improved inversion of scanning DMA data, *Aerosol Sci. Technol.*, *36*(1), 1–9, doi:10.1080/027868202753339032.

Decesari, S., M. Mircea, F. Cavalli, S. Fuzzi, F. Moretti, E. Tagliavini, and M. C. Facchini (2007), Source attribution of water-soluble organic aerosol by nuclear magnetic resonance spectroscopy, *Environ. Sci. Technol.*, *41*, 2479–2484, doi:10.1021/es0617111.

Duplissy, J., et al. (2008), Cloud forming potential of secondary organic aerosol under near atmospheric conditions, *Geophys. Res. Lett.*, *35*, L03818, doi:10.1029/2007GL031075.

Dusek, U., et al. (2005), "Missing" cloud condensation nuclei in peat smoke, *Geophys. Res. Lett.*, *32*, L11802, doi:10.1029/2005GL022473.

Dusek, U., G. P. Reischl, and R. Hitzenberger (2006), CCN activation of pure and coated carbon black particles, *Environ. Sci. Technol.*, *40*(4), 1223–1230, doi:10.1021/es0503478.

Flagan, R. C. (1999), On differential mobility analyzer resolution, *Aerosol Sci. Technol.*, *30*(6), 556–570, doi:10.1080/027868299304417.

Fletcher, N. H. (1958), Size effects in heterogeneous nucleation, *J. Chem. Phys.*, *29*(3), 572–576, doi:10.1063/1.1744540.

Frank, G. P., U. Dusek, and M. O. Andreae (2006), Technical note: A method for comparing size-resolved CCN in the atmosphere, *Atmos. Chem. Phys. Discuss.*, *6*, 4879–4895.

Glenn, E. P., J. J. Brown, and E. Blumwald (1999), Salt tolerance and crop potential of halophytes, *Crit. Rev. Plant Sci.*, *18*(2), 227–255, doi:10.1016/S0735-2689(99)00388-3.

Gorham, J., R. G. W. Jones, and E. McDonnell (1985), Some mechanisms of salt tolerance in crop plants, *Plant Soil*, *89*(1–3), 15–40, doi:10.1007/BF02182231.

Gunthe, S. S., et al. (2009), Cloud condensation nuclei in pristine tropical rainforest air of Amazonia: Size-resolved measurements and modeling of

atmospheric aerosol composition and CCN activity, *Atmos. Chem. Phys.*, *9*, 7551–7575.

Gysel, M., G. B. McFiggans, and H. Coe (2009), Inversion of tandem differential mobility analyser (TDMA) measurements, *J. Aerosol Sci.*, *40*, 134–151, doi:10.1016/j.jaerosci.2008.07.013.

Hopkins, R. J., K. Lewis, Y. Desyaterik, Z. Wang, A. V. Tivanski, W. P. Arnott, A. Laskin, and M. K. Gilles (2007), Correlations between optical, chemical and physical properties of biomass burn aerosols, *Geophys. Res. Lett.*, *34*, L18806, doi:10.1029/2007GL030502.

Huff Hartz, K. E. H., J. E. Tischuk, M. N. Chan, C. K. Chan, N. M. Donahue, and S. N. Pandis (2006), Cloud condensation nuclei activation of limited solubility organic aerosol, *Atmos. Environ.*, *40*(4), 605–617, doi:10.1016/j.atmosenv.2005.09.076.

Kandlikar, M., and G. Ramachandran (1999), Inverse methods for analysing aerosol spectrometer measurements: A critical review, *J. Aerosol Sci.*, *30*(4), 413–437, doi:10.1016/S0021-8502(98)00066-4.

Kaufmann, Y. J., et al. (1998), Smoke, Clouds, and Radiation-Brazil (SCAR-B) experiment, *J. Geophys. Res.*, *103*(D24), 31,783–31,808.

King, S. M., T. Rosenørn, J. E. Shilling, Q. Chen, and S. T. Martin (2009), Increased cloud activation potential of secondary organic aerosol for atmospheric mass loadings, *Atmos. Chem. Phys.*, *9*, 2959–2971.

Knutson, E. O., and T. B. Whitby (1975), Aerosol classification by electric mobility: Apparatus, theory, and applications, *J. Aerosol Sci.*, *6*, 443–451, doi:10.1016/0021-8502(75)90060-9.

Kreidenweis, S. M., K. Koehler, P. J. DeMott, A. J. Prenni, C. Carrico, and B. Ervens (2005), Water activity and activation diameters from hygroscopicity data: Part I: Theory and application to inorganic salts, *Atmos. Chem. Phys.*, *5*, 1357–1370.

Lance, S., J. Medina, J. N. Smith, and A. Nenes (2006), Mapping the operation of the DMT Continuous Flow CCN counter, *Aerosol Sci. Technol.*, *40*(4), 242–254, doi:10.1080/02786820500543290.

Lee, Y. S., D. R. Collins, L. Runjun, K. P. Bowman, and G. Feingold (2006), Expected impact of aged biomass burning aerosol on cloud condensation nuclei and droplet concentrations, *J. Geophys. Res.*, *111*, D22204, doi:10.1029/2005JD006464.

Lewis, K. A., et al. (2009), Reduction in biomass burning aerosol light absorption upon humidification: Roles of inorganically induced hygroscopicity, particle collapse, and photoacoustic heat and mass transfer, *Atmos. Chem. Phys. Discuss.*, *9*, 15,247–15,294.

Lin, J. C., T. Matsui, R. A. Pielke, and C. Kummerow (2006), Effects of biomass-burning-derived aerosols on precipitation and clouds in the Amazon Basin: A satellite-based empirical study, *J. Geophys. Res.*, *111*, D19204, doi:10.1029/2005JD006884.

Mahata, P. C., and D. J. Alofs (1975), Insoluble condensation nuclei: The effect of contact angle, surface roughness and adsorption, *J. Atmos. Sci.*, *32*, 116–122, doi:10.1175/1520-0469(1975)032<0116:ICNTEO>2.0.CO;2.

McMeeking, G. (2008), The optical, chemical, and physical properties of aerosol and gases emitted by laboratory combustion of wildland fuels, Ph.D. thesis, 312 pp., Colo. State Univ., Fort Collins.

McMeeking, G. R., et al. (2009), Emissions of trace gases and aerosols during the open combustion of biomass in the laboratory, *J. Geophys. Res.*, *109*, D19210, doi:10.1029/2009JD011836.

Mochida, M., and K. Kawamura (2004), Hygroscopic properties of levoglucosan and related organic compounds characteristic to biomass burning aerosol particles, *J. Geophys. Res.*, *109*, D21202, doi:10.1029/2004JD004962.

Moosmüller, H., R. K. Chakrabarty, and W. P. Arnott (2009), Aerosol light absorption and its measurement: A review, *J. Quant. Spectrosc. Radiat. Transfer*, *110*, 844–878, doi:10.1016/j.jqsrt.2009.1002.1035.

Novakov, T., and C. E. Corrigan (1996), Cloud condensation nucleus activity of the organic component of biomass smoke particles, *Geophys. Res. Lett.*, *23*(16), 2141–2144, doi:10.1029/96GL01971.

Petters, M. D., and S. M. Kreidenweis (2007), A single parameter representation of hygroscopicity growth and cloud condensation nucleus activity, *Atmos. Chem. Phys.*, *7*, 1961–1971.

Petters, M. D., A. J. Prenni, S. M. Kreidenweis, P. J. DeMott, A. Matsunaga, Y. B. Lim, and P. J. Ziemann (2006), Chemical aging and the hydrophobic-to-hydrophilic conversion of carbonaceous aerosol, *Geophys. Res. Lett.*, *33*, L24806, doi:10.1029/2006GL027249.

Petters, M. D., A. J. Prenni, S. M. Kreidenweis, and P. J. DeMott (2007), On measuring the critical diameter of cloud condensation nuclei using mobility selected aerosol, *Aerosol Sci. Technol.*, *41*(10), 907–913.

Petters, M. D., et al. (2009a), Ice nuclei emissions from biomass burning, *J. Geophys. Res.*, *114*, D07209, doi:10.1029/2008JD011532.

Petters, M. D., H. Wex, E. Hallberger, L. Poulain, C. M. Carrico, G. McMeeking, S. M. Kreidenweis, F. Stratmann, and A. Massling (2009b), Towards closing the gap between hygroscopic growth and activation for secondary organic aerosol: Part II. Theoretical approaches, *Atmos. Chem. Phys.*, *9*, 3999–4009.

Posfai, M., R. Simonics, J. Li, P. V. Hobbs, and P. R. Buseck (2003), Individual aerosol particles from biomass burning in southern Africa: 1. Compositions and size distributions of carbonaceous particles, *J. Geophys. Res.*, *108*(D13), 8483, doi:10.1029/2002JD002291.

Prenni, A. J., P. J. DeMott, S. M. Kreidenweis, D. E. Sherman, L. M. Russell, and Y. Ming (2001), The effects of low molecular weight dicarboxylic acids on cloud formation, *J. Phys. Chem. A*, *105*(50), 11,240–11,248, doi:10.1021/jp012427d.

Prenni, A. J., M. D. Petters, P. J. DeMott, S. M. Kreidenweis, P. J. Ziemann, A. Matsunaga, and Y. B. Lim (2007), Cloud droplet activation of secondary organic aerosol, *J. Geophys. Res.*, *112*, D10223, doi:10.1029/2006JD007963.

Raymond, T. M., and S. N. Pandis (2002), Cloud activation of single-component organic aerosol particles, *J. Geophys. Res.*, *107*(D24), 4787, doi:10.1029/2002JD002159.

Reid, J. S., and P. V. Hobbs (1998), Physical and optical properties of young smoke from individual biomass fires in Brazil, *J. Geophys. Res.*, *103*(D24), 32,013–32,030.

Rissler, J., A. Vestin, E. Swietlicki, G. Fisch, J. Zhou, P. Artaxo, and M. O. Andreae (2006), Size distribution and hygroscopic properties of aerosol particles from dry-season biomass burning in Amazonia, *Atmos. Chem. Phys.*, *6*, 471–491.

Roberts, G. C., and A. Nenes (2005), A continuous-flow streamwise thermal-gradient CCN chamber for atmospheric measurements, *Aerosol Sci. Technol.*, *39*(3), 206–221, doi:10.1080/027868290913988.

Rogers, C. F., J. Hudson, B. Zielinska, R. L. Tanner, J. Hallet, and J. G. Watson (1991), Cloud condensation nuclei from biomass burning, in *Global Biomass Burning: Atmospheric, Climatic, and Biospheric Implications*, edited by J. S. Levine, pp. 431–438, MIT Press, Cambrige, Mass.

Rose, D., S. S. Gunthe, E. Mikhailov, G. P. Frank, U. Dusek, M. O. Andrea, and U. Pöschl (2008a), Calibration and measurement uncertainties of a continuous-flow cloud condensation nuclei counter (DMT-CCNC): CCN activation of ammonium sulfate and sodium chloride aerosol particles in theory and experiment, *Atmos. Chem. Phys.*, *8*, 1153–1179.

Rose, D., A. Nowak, P. Achert, A. Wiedensohler, M. Hu, M. Shao, Y. Zhang, M. O. Andrea, and U. Pöschl (2008b), Cloud condensation nuclei in polluted air and biomass burning smoke near the mega-city Guangzhou, *Atmos. Chem. Phys. Discuss.*, *8*, 17,343–17,392.

Rosenørn, T., G. Kiss, and M. Bilde (2006), Cloud droplet activation of saccharides and levoglucosan particles, *Atmos. Environ.*, *40*(10), 1794–1802, doi:10.1016/j.atmosenv.2005.11.024.

Ross, K. E., S. J. Piketh, R. T. Bruintjes, R. P. Burger, R. J. Swap, and H. J. Annegarn (2003), Spatial and seasonal variations in CCN distribution and the aerosol-CCN relationship over southern Africa, *J. Geophys. Res.*, *108*(D13), 8481, doi:10.1029/2002JD002384.

Sassen, K., and V. I. Khvorostyanov (2008), Cloud effects from boreal forest fire smoke: Evidence for ice nucleation from polarization lidar data and cloud model simulations, *Environ. Res. Lett.*, *3*(2), 025006, doi:10.1088/1748-9326/3/2/025006.

Shantz, N. C., W. R. Leaitch, L. Phinney, D. Toom-Sauntry, and M. Mozurkewich (2008), The effect of organic compounds on the growth rate of cloud droplets in marine and forest settings, *Atmos. Chem. Phys.*, *8*, 5869–5887.

Sjogren, S., M. Gysel, E. Weingartner, U. Baltensperger, M. J. Cubison, H. Coe, A. A. Zardini, C. Marcolli, U. K. Krieger, and T. Peter (2007), Hygroscopic growth and water uptake kinetics of two-phase aerosol particles consisting of ammonium sulfate, adipic and humic acid mixtures, *J. Aerosol Sci.*, *38*(2), 157–171, doi:10.1016/j.jaerosci.2006.11.005.

Stolzenburg, M., and P. H. McMurry (1988), TDMAfit user's manual, *PTL Publ. 653*, Particle Technol. Lab., Dep. of Mech. Eng., Univ. of Minn. At Minneapolis, Minneapolis.

Stratmann, F., T. Kauffeldt, D. Hummes, and F. Fissan (1997), Differential electrical mobility analysis: A theoretical study, *J. Aerosol Sci.*, *26*(4), 368–383, doi:10.1080/02786829708965437.

Svenningsson, B., et al. (2006), Hygroscopic growth and critical supersaturations for mixed aerosol particles of inorganic and organic compounds of atmospheric relevance, *Atmos. Chem. Phys.*, *6*, 1937–1952.

Swietlicki, E., et al. (2008), Hygroscopic properties of submicrometer atmospheric aerosol particles measured with H-TDMA instruments in various environments—A review, *Tellus, Ser. B*, *60*(3), 432–469, doi:10.1111/j.1600-0889.2008.00350.x.

Vestin, A., J. Rissler, E. Swietlicki, G. P. Frank, and M. O. Andreae (2007), Cloud-nucleating properties of the Amazonian biomass burning aerosol: Cloud condensation nuclei measurements and modeling, *J. Geophys. Res.*, *112*, D14201, doi:10.1029/2006JD008104.

Wang, J., Y. N. Lee, P. H. Daum, J. Jayne, and M. L. Alexander (2008), Effects of aerosol organics on cloud condensation nucleus (CCN) concentration and first indirect aerosol effect, *Atmos. Chem. Phys.*, *8*(21), 6325–6339.

Wiedensohler, A. (1988), An approximation of the bipolar charge-distribution for particles in the sub-micron size range, *J. Aerosol Sci.*, *19*(3), 387–389, doi:10.1016/0021-8502(88)90278-9.

Zhou, J., E. Swietlicki, H. C. Hansson, and P. Artaxo (2002), Submicrometer aerosol particle size distribution and hygroscopic growth measured in the Amazon rain forest during the wet season, *J. Geophys. Res.*, *107*(D20), 8055, doi:10.1029/2000JD000203.

Ziese, M., H. Wex, E. D. Nilsson, I. Salma, R. Ocskay, T. Hennig, A. Massling, and F. Stratmann (2008), Hygroscopic growth and activation of HULIS particles: Experimental data and a new iterative parameterization scheme for complex aerosol particles, *Atmos. Chem. Phys.*, *8*, 1855–1866.

C. M. Carrico, J. L. Collett Jr., P. J. DeMott, S. M. Kreidenweis, and A. J. Prenni, Department of Atmospheric Science, Colorado State University, Fort Collins, CO 80523, USA.

H. Moosmüller, Desert Research Institute, Nevada System of Higher Education, Reno, NV 89512, USA.

M. D. Petters, Department of Marine Earth and Atmospheric Sciences, North Carolina State University, Campus Box 8208, Raleigh, NC 27695-8208, USA. (markus_petters@ncsu.edu)